

A PAM-4 100 Gbps Single-Drive Strained SiGe Optical Lumped Mach-Zehnder Modulator for O-Band Application

Youngjoo Bae^{ID}, Seong Ui An^{ID}, Taewon Jin, and Younghyun Kim^{ID}

Abstract—We propose the carrier-depletion type strained SiGe optical lumped Mach-Zehnder modulators (MZMs) with L-shape PN junction (LSPN) with a highly CMOS-compatible fabrication method. The device performance is numerically investigated and optimized by technology computer-aided design (TCAD) simulation. The optimized SiGe LSPN MZ modulator exhibits a high modulation efficiency of 0.52 Vcm for $V_{\pi}L$ with reverse bias voltages of 0V to −2V at 1310 nm wavelength, which is 3.5 times smaller than the conventional PN junction device thanks to strained SiGe. Furthermore, we carried out the large-signal simulation with 1-mW input power. As a result, we found that the SiGe LSPN MZ modulator can achieve 0.54 mW (−2.7 dBm) and 0.17 mW (−7.7 dBm) eye-openings for 50-Gbps NRZ-OOK and 100-Gbps PAM-4, respectively, taking advantage of single-drive configuration and optimizing input characteristics impedance. We expect this SiGe lumped MZ modulator can be one of the promising solutions for replacing a very long Si MZ modulator with traveling-wave electrodes.

Index Terms—Strained SiGe, optical modulation, PAM-4, Mach-Zehnder modulator.

I. INTRODUCTION

SILICON (Si) photonics is one of the most promising integrated photonics platforms leveraging the existing Si CMOS technology. Its development has been mainly driven by the need for high-speed optical interconnects in data centers and high-performance computing systems to address the bottleneck of ever-increasing data traffic [1], [2], [3], [4], [5]. Recently, Si photonic optical transceivers have been commercialized for the data center application and their usage is expected to increase more and more with the demands of the traffic due to the technological revolution of artificial intelligence, big data, internet-of-things, AR/VR, etc.

Manuscript received 9 June 2023; revised 30 August 2023; accepted 7 September 2023. Date of publication 25 September 2023; date of current version 26 October 2023. This work was supported in part by the Technology Innovation Program through the Korea Evaluation Institute of Industrial Technology (KEIT) funded by the Ministry of Trade, Industry & Energy (MOTIE), South Korea, under Grant 20015909; in part by the National Research Foundation of Korea (NRF) funded by the Korean Government [Ministry of Science and ICT (MSIT)] under Grant 2022K1A3A1A79090726; in part by the Korea Basic Science Institute (National Research Facilities and Equipment Center) funded by the Ministry of Education under Grant 2023R1A6C103A035 and Grant 2021R1A6C101A405; and in part by the Integrated Circuit (IC) Design Education Center. (Corresponding author: Younghyun Kim.)

The authors are with the Department Photonics and Nanoelectronics, Hanyang University, Ansan 15588, South Korea (e-mail: younghyunkim@hanyang.ac.kr).

Color versions of one or more figures in this article are available at <https://doi.org/10.1109/JQE.2023.3318587>.

Digital Object Identifier 10.1109/JQE.2023.3318587

Among the necessary building blocks consisting of the optical interconnect, an optical modulator plays a very important role, particularly for the high-speed data rate. For Si optical modulators in the technology platform, the plasma dispersion effect in Si is the main principle for optical phase shift [6]. The depletion-type Si Mach-Zehnder optical modulators based on the effect have been mostly used for high-speed modulation and broad-wavelength operation [7], [8], [9]. However, the carrier-depletion Si modulators need a relatively long phase-shifter or high driving voltage because Si has a weak plasma dispersion effect due to the limitation of the optical material [10], [11], [12]. Also, it requires an additional and complicated design of a traveling-wave electrode for RF transmission to the long phase-shifter, while a lumped modulator, with a phase-shifter length is approximately 500 μm or less, can be operated with a simple electrode because RF signals are minimally impacted by the phase shifter length.

To address this problem, heterogeneous integration approaches have been investigated, introducing two-dimensional materials (e.g. graphene [13], [14], WSe₂ [15], [16]), ceramic materials (e.g. BTO [17], LN [18], [19], KTN [20]), III-V compounds materials [21] into hybrid optical modulators. However, it degrades the advantage of Si Photonics because they are less CMOS compatible. In terms of that, strained SiGe is highly CMOS compatible [22] because it has long been used in CMOS technology [23] and is currently used in the gate-all-around (GAA) process [24]. In addition, SiGe modulators [25] and Ge detectors [26] have been successfully demonstrated in Si Photonics technology. Therefore, our approach can also be utilized for optical communications systems. More importantly, it is also a promising material for the improvement of the modulator performance by enhancing the plasma dispersion effect [11], [22], [27], [28], [29], [30], [31]. The strained SiGe has a much lower effective mass of holes than that of Si, resulting in a larger plasma dispersion effect. Several PN modulators using strained SiGe have been reported and have shown high efficiency [32], [33], [34], [35]. One of them, the strained SiGe modulator with a vertical PN junction shows the result of $V_{\pi}L$ is 0.31 Vcm, 1.8 times lower than the Si optical modulator, thanks to not only the strained SiGe but also the geometrical effect of the vertical PN junction (larger mode overlap between the optical mode and larger junction area) [36]. Nevertheless, the proposed device has not been experimentally demonstrated so far. The main reason

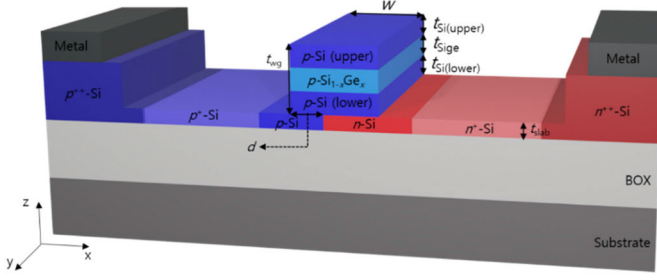


Fig. 1. Proposed cross-sectional device structure of carrier-depletion type strained SiGe optical modulator with L-shape PN junction.

should be the unfavored fabrication process of the vertical PN junction which requires additional top Si growth [36]. On the other hand, studies on technology computer-aided design (TCAD) simulation [37], [38], [39] and experimental demonstrations [40], [41], [42] of L, U, and S-shaped PN junction optical modulators have been reported. It overcomes the drawback of the vertical junction with a simple fabrication method maintaining the modulation efficiency resulting from an advantageous geometrical effect.

Numerous modulators that utilize only Si and achieve lower $V_{\pi}L$ through simpler fabrication processes have also been investigated [37], [40], [41], [42]. When considering only $V_{\pi}L$, increasing the junction area can achieve a lower $V_{\pi}L$. However, there is a drawback wherein the operational speed might be compromised due to the trade-off relationship between junction area and capacitance. By utilizing SiGe, it is possible to achieve a lower $V_{\pi}L$ while maintaining capacitance and loss thanks to the enhanced plasma dispersion effect in strained SiGe.

In this study, we propose the strained SiGe depletion-type optical modulator with LSPN for further improvement as shown in Fig. 1. We analyze and optimize the modulation characteristics depending on the process and design parameters at 1310 nm for datacom application using TCAD simulation. Finally, we present the feasible implementations of single-drive 50-Gbps NRZ-OOK and 100-Gbps PAM-4 data transmission of SiGe LSPN lumped MZ modulators.

II. PROPOSED DEVICE STRUCTURE AND SIMULATION METHOD

First, we introduce our proposed device. Figure 1 presents a schematic of the proposed depletion-type strained SiGe optical modulator with a L-shape PN (LSPN) junction. The Si waveguide width (w) is 400 nm designed for the O-band application. The mesa (t_{wg}) is 160 nm and the Si slab thickness (t_{slab}) is 60 nm. In the mesa, the rib waveguide consists of heterostructure Si/SiGe/Si layers in which the thickness is 20 nm for the bottom p -Si layer ($t_{Si(lower)}$), 15 nm for the p -SiGe (t_{SiGe}) layer, and 125 nm for the top p -Si layer ($t_{Si(upper)}$), respectively. The Ge mole fraction is 20% so that it can avoid material absorption loss for O-band application [43]. Si regions in the slab are p -type or n -type doped, and their doping levels are very heavy (p^{++} -Si and n^{++} -Si, $\sim 10^{20} \text{ cm}^{-3}$) for ohmic contact, heavy (p^{+} -Si and n^{+} -Si,

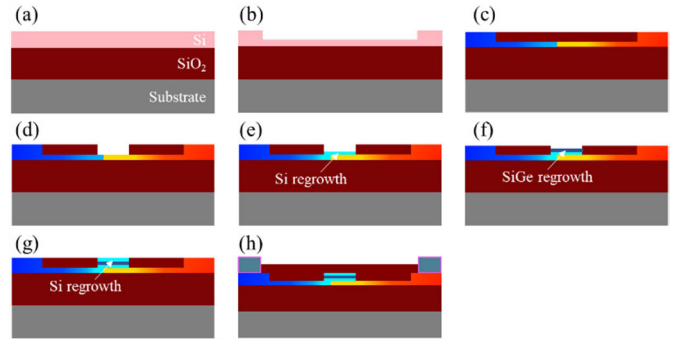


Fig. 2. Process fabrication flow of strained SiGe optical modulator with L-shape PN junction, (a) SOI substrate, (b) Slab formation, (c) SiO₂ passivation and PN junction formation, (d) SiO₂ etching for rib waveguide formation, (e) Si regrowth, (f) Si_{1-x}Ge_x regrowth, (g) Si regrowth, and (h) Metal electrode formation.

$\sim 10^{19} \text{ cm}^{-3}$) for low series resistance, and light (p -Si and n -Si are $5 \times 10^{17} \text{ cm}^{-3}$ and $1 \times 10^{18} \text{ cm}^{-3}$, respectively) for optical phase shift. The length of the gap (d) is 70 nm, which is the distance between the left-hand edge of the Si waveguide and the left-hand edge of the phosphorus implantation region, n -Si. In addition, the doping level of p -Si(lower), p -SiGe, p -Si(upper) regions are $1.4 \times 10^{18} \text{ cm}^{-3}$, $8 \times 10^{17} \text{ cm}^{-3}$, and $0.5 \times 10^{17} \text{ cm}^{-3}$, respectively. It is important to notice the four important parameters mainly attributing to the modulation efficiency, which are the distance (d), hole concentration of the SiGe layer, and the thickness of the two layers of Si(lower) and SiGe represented by $t_{Si(lower)}$ and t_{SiGe} . Those parameters will be discussed when describing the modulator performance optimization.

As we mentioned, our proposed device can be more easily fabricated compared to the vertical PN junction modulators [36]. To address it, we present the fabrication flow of the device in Fig. 2. The Si slab is first formed by dry etching, whose thickness is 60 nm in Fig. 2(a) and 2(b). Before ion implantation, the passivation layer of SiO₂ is deposited followed by planarization by CMP. As shown in Fig. 2(c), the slab and contact regions are doped with the doping conditions mentioned above. After that, it is notable that the high-temperature activation annealing should be carried out before strained SiGe formation. Because the strained SiGe is in a metastable state, relaxation induced by various processes, particularly higher temperatures than its thermal budget, can lead to a reduction in the enhancement of strained SiGe. Therefore, the thermal budget of strained SiGe should be carefully considered when it is integrated into a Si photonics platform. Then, the SiO₂ is dry-etched for the Si/SiGe/Si waveguide formation. Fig. 2(e), 2(f), and 2(g) show epitaxial Si/SiGe/Si heterostructure growth, respectively. Since we target the waveguide thickness of 220 nm, we have further epitaxy-grown Si on the SiGe layer to increase the overlap between the optical mode and the SiGe layer. For the target hole concentration, it is possible to use the *in-situ* doping technique while growing the Si/SiGe/Si. Finally, the metal electrodes for the cathode and anode are constructed as shown in Fig. 2(h). Since the strong plasma dispersion effect in SiGe is obtained by using the hole effective mass of strained SiGe,

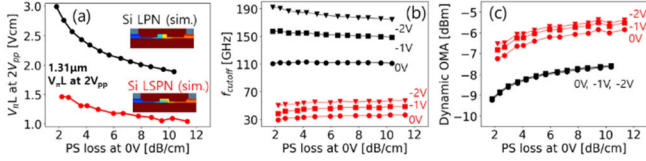


Fig. 3. (a) $V_{\pi}L$ (b) f_{cutoff} and (c) OMA of Si LPN and Si LSPN optical modulator as a function of PS-loss at 0V.

LSPN must be formed in p -type SiGe on top of n -type Si to use holes in the proposed structure.

To simulate the optical characteristics of modulators, we used Synopsys TCAD Sentaurus to calculate the carrier concentration and Ansys Lumerical optical mode solver. The carrier concentration was calculated as a function of the applied DC reverse bias between the p^{++} and n^{++} contact metals. We assume ohmic contact to the p^{++} and n^{++} regions with a peak doping concentration at the surface of $\sim 10^{20} \text{ cm}^{-3}$ for boron and phosphorus, respectively [38]. For the plasma dispersion effect in Si, an updated Soref's equation was used [44]. We previously verified our TCAD simulation setup for Si optical phase shifters to the PDK device specification of IMEC's ISIPP50G platform [21], [45]. For strained SiGe, the enhancement factors for the changes in the refractive index and absorption coefficient were used to simulate the modulation performance [12] as we previously reported using the same method [36]. Also, details on our simulation method, which has been calibrated and verified well, can be found in the previous work [38].

III. MODULATION PERFORMANCE OPTIMIZATION

A. Optimization of the Proposed SiGe Mach-Zehnder Modulator

In this section, we present modulation performance optimization of the proposed LSPN strained SiGe optical modulator with important design parameters. Prior to discussing the strained SiGe optical modulator, we show the TCAD simulation results of the Si lateral PN junction (LPN) and LSPN optical modulators for $1.31 \mu\text{m}$ in Fig. 3. The free-carriers are important parameters for $V_{\pi}L$ and PS loss, which is controlled by the doping conditions in the pn-junction located rib. So, the simulated results in Fig. 3 were obtained by increasing the doping concentration in the waveguide rib. Details such as ion implantation process conditions are given in our previous work [38]. The $V_{\pi}L$ and PS loss at 0 V in the tradeoff relationship is shown in Fig. 3(a). As expected by the previous work for C-band application [38], Si LSPN shows larger modulation efficiency than Si LPN due to a larger overlap between the optical mode and depletion region. In Fig. 3(b), the cutoff frequency (f_{cutoff}) of LSPN is smaller than that of LPN due to the large C_j , which is calculated by $f_{cutoff} = 1/(2\pi R_s C_j)$. Although the lower frequency will limit the high-speed operation, it can be compensated by the single-drive configuration. The two MZM arms' capacitances are connected in series; hence, the C_j can be reduced by half, resulting in the higher compensated cutoff frequency as reported in [38] and [46]. Figure 3(c) shows the dynamic optical modulation amplitude (OMA) of Si LPN and Si LSPN

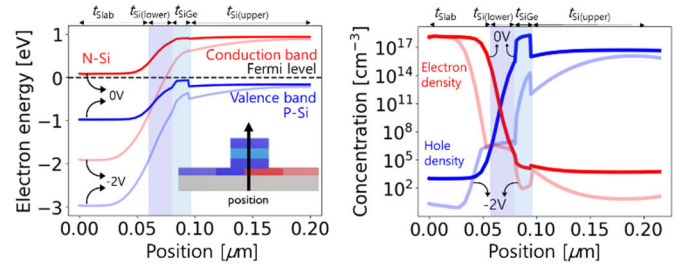


Fig. 4. (a) Band structure, and (b) carrier distribution in z -direction at the center of the waveguide.

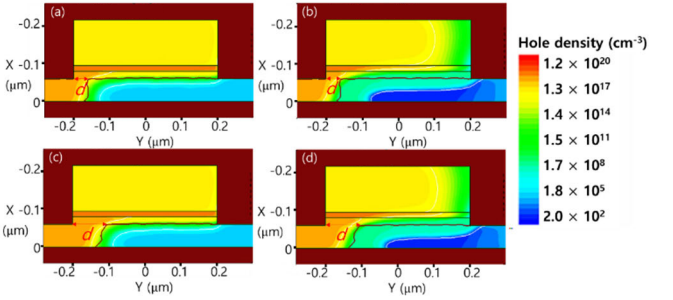


Fig. 5. Cross-sectional device structure of SiGe optical phase shifter of (a) and (b) $d = 60 \text{ nm}$ at bias = 0 and -2V , (c) and (d) $d = 100 \text{ nm}$ at bias = 0 and -2V , respectively.

at 0 V, -1 V , and -2 V for the 50-Gbps target data rate, which can be calculated by the model [38] and parameters of $V_{\pi}L$, loss, f_{cutoff} . The dynamic OMA values of Si LPN and Si LSPN are -7.5 dBm and -6.5 to -5.5 dBm at 10 dB/cm , respectively. The variable values of Si LSPN with bias voltages are caused by the variable and low frequency for the target data rate, while Si LPN's cutoff frequency is not because it is high enough.

The proposed SiGe device has the Si/SiGe/Si heterostructure in the waveguide core. The SiGe's bandgap is smaller than that of Si. It causes a large band offset in the valence band, which is an important key to improving device performance using holes in the strained SiGe layer. Fig. 4(a) and 4(b) show band structure and carrier distribution in the z -direction at the center of the waveguide when 0 V and -2 V are applied to the anode while the cathode is grounded, respectively. The PN junction is formed between n -Si and p -Si, showing the large band bending across the heterostructure. It is notable that holes are confined in the SiGe well due to the band offset. When the reverse bias is applied, it can be seen from the band structure that depletion starts to occur in the Si and SiGe layers and the hole density in the strained SiGe layer remarkably decreases. It means that the modulation efficiency is expected to be further enhanced by confining more holes in the strained SiGe layer where the plasma dispersion is greater than Si.

First, we investigated the d dependency on device performance because the d geometrically affects the junction area and device performance. Fig. 5 illustrates the two-dimensional hole density profile of the Si/SiGe/Si waveguide core for 60- and 100-nm-wide d at 0 and -2 V , respectively. The change in d causes a change in the depletion area of the SiGe layer in the waveguide core, where the depletion

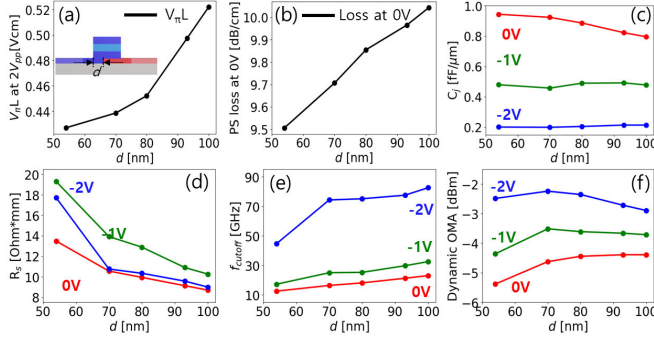


Fig. 6. (a) $V_{\pi}L$ (b) Phase shifter loss at 0V, (c) junction capacitance, (d) series resistance, (e) f_{cutoff} and (f) OMA of SiGe optical modulator as a function of d .

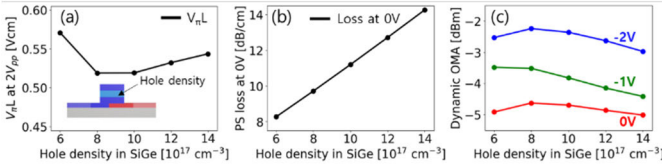


Fig. 7. (a) $V_{\pi}L$ (b) Phase shifter loss at 0V, and (c) OMA of strained SiGe optical modulator as a function of hole density in SiGe layer.

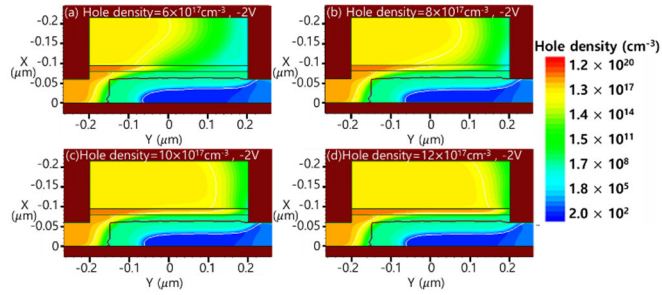


Fig. 8. Cross-sectional device structure of SiGe optical modulator at -2 V with various hole densities in SiGe of (a) $6 \times 10^{17} \text{ cm}^{-3}$ (b) $8 \times 10^{17} \text{ cm}^{-3}$ (c) $10 \times 10^{17} \text{ cm}^{-3}$ and (d) $12 \times 10^{17} \text{ cm}^{-3}$, bias = -2V.

area refers to the part enclosed by a white line. Fig. 6 shows electrical and optical characteristics for the strained SiGe optical modulator as a function of the d . As d increases, the overlap between the depletion region and the optical mode in the waveguide decreases; therefore, $V_{\pi}L$ increases indicating the lower modulation efficiency in Fig. 6(a). The phase-shifter (PS) loss at 0V shows increase with an increase in d in Fig. 6(b). As the d increases, the depletion region decreases, resulting in an increase in the hole density in the region where the optical mode is strongly confined. However, the capacitance exhibits a slight decrease, as shown in Fig. 6(c). Fig. 6(d) shows that the resistance decreases with an increase in d . Fig. 6(e) shows the f_{cutoff} calculated by the equation mentioned above. The f_{cutoff} is dependent on a bias voltage as well as d , caused by the behavior of C_j and R_s . The dynamic OMA values at each bias voltage were also calculated as shown in Fig. 6(f). As a result, the OMA can be optimized when the gap length is 70 nm.

Since the hole density in SiGe greatly affects the device performance, we also optimized it for the dynamic OMA. Fig. 7 shows $V_{\pi}L$, PS loss, and dynamic OMA as a function of the hole density in the strained SiGe layer as the inset

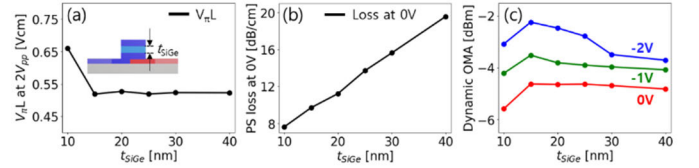


Fig. 9. (a) $V_{\pi}L$ (b) Phase shifter loss at 0V, and (c) OMA of strained SiGe optical modulator as a function of t_{SiGe} .

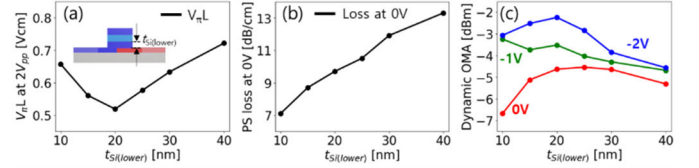


Fig. 10. (a) $V_{\pi}L$ (b) Phase shifter loss at 0V, and (c) OMA of strained SiGe optical modulator as a function of $t_{\text{Si(lower)}}$.

schematic in Fig. 7(a) indicates. As the hole concentration in the SiGe layer increases, the amount of change in the carrier concentration increases but the depletion width decreases as shown in Fig. 8. It results in the optimum $V_{\pi}L$ in the hole density range of 8 to $10 \times 10^{17} \text{ cm}^{-3}$. In Fig. 7(b), PS loss increases as increasing the hole concentration due to free carrier absorption. We also estimated the dynamic OMA considering f_{cutoff} in the same way. The dynamic OMA can be optimized with the hole density of $8 \times 10^{17} \text{ cm}^{-3}$ as shown in Fig. 7(c).

Next, we optimize the thickness of the SiGe layer. Since the highly doped SiGe is much lossier than the low doped Si(upper), the SiGe thickness should be designed as thin as possible, considering the depletion width at $2V_{\text{pp}}$. As shown in Fig. 9(a) and (b), the 15-nm-thickness SiGe layer is proper because $V_{\pi}L$ decreases and stagnates, but the loss increases with an increase in the thickness of SiGe. As can also be seen in Fig. 9(c), the OMA also presents the optimum value at the same thickness.

Fig. 10 presents the following optimization process for $t_{\text{Si(lower)}}$. The initial depletion region exists at the PN junction even with no bias voltage. Therefore, an appropriate $t_{\text{Si(lower)}}$ under the SiGe layer is important to make sure that depletion starts from the SiGe layer when a reverse bias voltage is applied. Here, the thickness of the waveguide rib is fixed, so the $t_{\text{Si(upper)}}$ decreases as the $t_{\text{Si(lower)}}$ increases. In Fig. 10(a), the 20-nm $t_{\text{Si(lower)}}$ is optimized because carriers in SiGe are already depleted for thinner thicknesses, and carriers in Si start to deplete followed by those in SiGe for thicker thicknesses. As the $t_{\text{Si(lower)}}$, whose layer has a higher hole density than Si(upper), increases, the PS loss increases as shown in Fig. 10(b). Thus, the dynamic OMA as a function of Si (lower) layer thickness is optimized at 20 nm for $t_{\text{Si(lower)}}$ in Fig. 10(c).

B. Comparison of SiGe LSPN to Si LPN and LSPN Mach-Zehnder Modulators

Fig. 11 shows a comparison of the modulation characteristics at 1310 nm for Si LPN, Si LSPN, and SiGe LSPN lumped MZ modulators as a function of PS-loss at 0V. The $V_{\pi}L$ and

TABLE I
PERFORMANCE COMPARISON OF SI-BASED MODULATORS FOR O-BAND APPLICATIONS

Ref.	Material/ Junction type	Sim./ Exp.	α [dB/cm]	$V_{\pi}L$ [Vcm]	$\alpha V_{\pi}L$ [VdB]	Bandwidth [GHz]	Length [mm]	ER [dB]
[48]	Si/ Lateral	Exp.	23.6	2.43 (at -1V)	57.35	30 (EO S21, at 0V)	3	3.4
[49]	Si/ Lateral	Exp.	6 (at 0 V)	2.14 (at -2.5V)	34.24	28 (EO S21, at -1.25V)	2	3.9
[50]	Si/ Lateral	Exp.	25 (at 1.7V)	1.15 (at -3.5V)	28.75	18 (EO S21)	1	5
[51]	Si/ L-shape	Exp.	27 (at 0 V)	0.78 (at -2.6V)	21.06	20 (EO S21, at -3V)	3	5.5
This work	Si/ L-shape	Sim.	9.5 (at 0 V)	1.05 (at 0V to -2V)	9.98	35, 47, 55 (intrinsic, at 0V, -1V, -2V)	0.5	3
This work	SiGe/ L-shape	Sim.	9.7 (at 0 V)	0.52 (at 0V to -2V)	5.04	16, 25, 74 (intrinsic, at 0V, -1V, -2V)	0.5	6.4

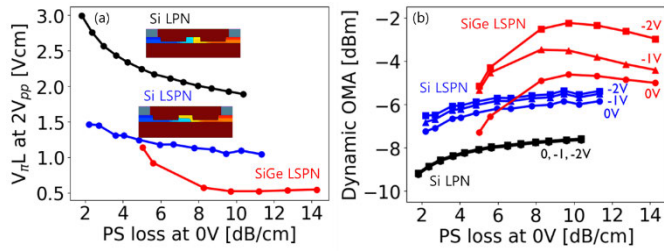


Fig. 11. (a) $V_{\pi}L$ and (b) OMA of Si LPN, Si LSPN and optimized SiGe LSPN lumped MZ modulators as a function of PS-loss at 0V.

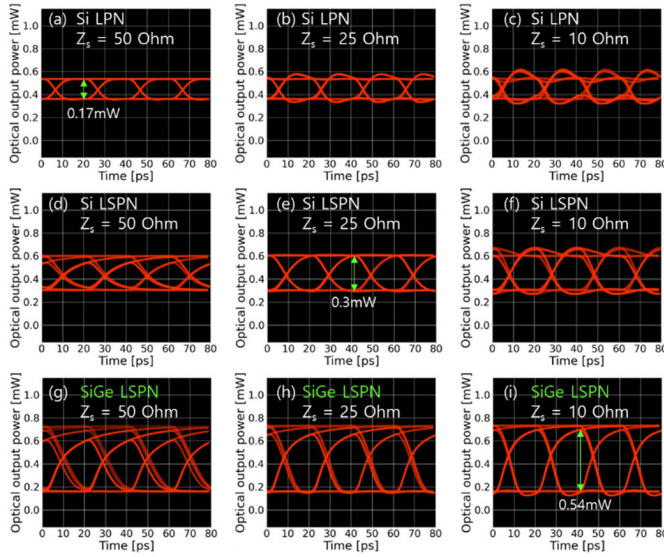


Fig. 12. Simulated eye diagram with $2^7 - 1$ pattern of SD configuration based Si LPN with (a) 50 Ohm, (b) 25 Ohm, (c) 10 Ohm, Si LSPN with (d) 50 Ohm, (e) 25 Ohm, (f) 10 Ohm, and SiGe LSPN with (g) 50 Ohm, (h) 25 Ohm, (i) 10 Ohm for 50 Gbps NRZ-OOK.

PS loss have a tradeoff relationship [38]. When the PS loss is around 10 dB/cm, the $V_{\pi}L$ value of the SiGe LSPN modulator is 0.52 Vcm, which is 3.5 times higher modulation efficiency than the conventional Si LPN modulator. The dynamic OMA is 0.45 mW (-3.5 dBm) at -1 V, which is 2.6 times higher than that of the Si LPN modulator.

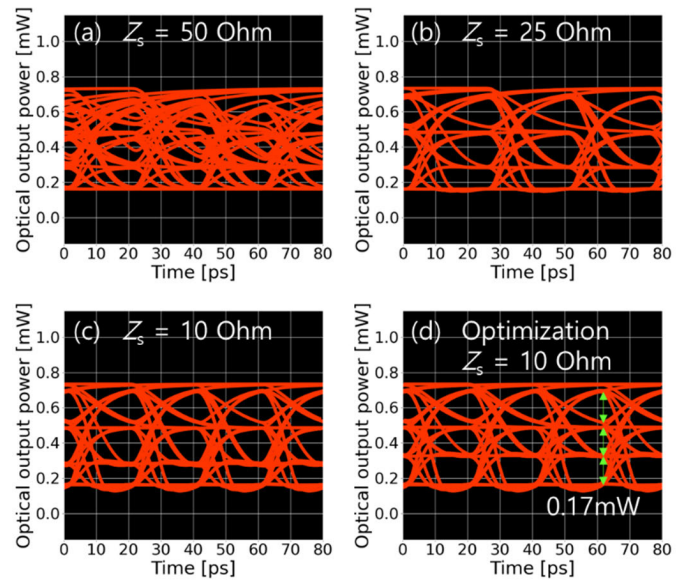


Fig. 13. PAM-4 100-Gbps eye diagram with $2^7 - 1$ pattern of SD configuration based proposed SiGe LSPN with (a) 50 Ohm, (b) 25 Ohm, (c) 10 Ohm, and (d) 10 Ohm with compensated voltage inputs.

C. Large-Signal Simulation of Si LPN, Si LSPN, and SiGe LSPN Lumped Mach-Zehnder Modulators

To quantitatively investigate the high-speed modulator performance, we implemented a large-signal simulation for Si LPN, LSPN, and SiGe LSPN lumped MZ modulators with 500- μ m PS length at the almost same loss (10 dB/cm) by the open-source electronic circuit simulator, Ngspice [47]. The simulation and verification methods in detail are found in our previous work [38]. The single-drive method is applied to compensate for the limited bandwidth due to the high capacitance value [46]. The input optical power is assumed to be 1 mW (0 dBm) and the input signal is PRBS $2^7 - 1$ pattern. Fig. 12 shows the simulated 50Gbps eye diagrams of the three modulators with different input impedances. Eye-opening varies depending on the Z_s value. The limited bandwidth can be further improved by reducing the input impedance. The largest eye-opening for Si LPN

and LSPN is estimated to be 0.17 mW (−7.7dBm) when $Z_5 = 50\Omega$ and 0.3 mW (−5.2dBm) when $Z_5 = 25\Omega$, respectively. The larger Z_5 shows the bandwidthlimited eye diagram and the smaller Z_5 shows unnecessary peaking. For SiGe LSPN, the largest eye-opening is expected to be 0.54 mW (−2.7dBm) when $Z_s = 10\Omega$ which is 3 times larger compared to Si LPN.

In addition, we implemented the 100 Gbps (50 Gbaud/s) PAM-4 operations for the SiGe LSPN MZ modulator with the single-drive scheme. We also simulated to improve the eye-opening by changing the impedance, as shown in Fig. 13. The clearest eye-opening is shown in Fig. 13(c) when the impedance is set to 10 Ω , as compared to higher impedance conditions of 50 Ω and 25 Ω in Fig. 13(b) and (c) respectively. However, the different eye-openings in Fig. 13(c) are caused by the nonlinearity of the device performance. To eliminate the nonlinearity, the compensated input voltages of 0, −1.3, −2.3, and −4 V are applied. As a result, we optimized PAM-4 with the same value of 0.17 mW (−7.7 dBm) in the 4-level in Fig. 13(d).

We show the performance comparison of Si-based MZ modulators for O-band applications in TABLE I. The junction type is included as the first column name. Then, the performance parameters are shown. We also include the matrix on which the performance result is based on simulation (Sim), and experiment (Exp). The performance metrics include optical PS loss per unit length, in dB/cm, modulation efficiency, represented by $V_\pi L$, the product of $V_\pi L$ and the phase-shifter loss, represented by $\alpha V_\pi L$, the intrinsic bandwidth of the phase shifter or reported −3 dB bandwidth of electro-optical S21 (EO S21) response, in GHz, phase shifter length in mm, extinction ratio that the ratio of the maximum and minimum value of the eye, represented by ER. The Si LSPN optical modulator has a lower $\alpha V_\pi L$ value than other reported Si LPN and LSPN optical modulators. The SiGe LSPN optical modulator shows a much lower $\alpha V_\pi L$ value than that. Thanks to the improved DC performance, the SiGe device presents an extinction ratio of 6.4 dB, which is higher than other reported devices in the TABLE I.

IV. CONCLUSION

The proposed SiGe LSPN optical modulator with high CMOS compatibility was numerically investigated in this study by TCAD simulation. We optimized the device performance, resulting in the $V_\pi L$ of 0.52 Vcm at 1310-nm wavelength, which is 3.5 times higher modulation efficiency than the conventional Si LPN modulator, thanks to strained SiGe. In addition, we performed the large-signal simulation with 1-mW input power. Consequently, it is found that the SiGe LSPN MZ modulator can achieve 0.54-mW (−2.7 dBm) and 0.17-mW (−7.7 dBm) eye-openings for 50-Gbps NRZ-OOK and 100-Gbps PAM-4, respectively, thanks to the single-drive configuration and the optimized input impedance. We believe that the SiGe lumped MZ modulator can be one of the promising solutions for replacing a very long Si MZ modulator with traveling-wave electrodes.

REFERENCES

- [1] D. Thomson et al., “Roadmap on silicon photonics,” *J. Opt.*, vol. 18, no. 7, Jun. 2016, Art. no. 073003, doi: [10.1088/2040-8978/18/7/073003](#).
- [2] X. Chen et al., “The emergence of silicon photonics as a flexible technology platform,” *Proc. IEEE*, vol. 106, no. 12, pp. 2101–2116, Dec. 2018, doi: [10.1109/JPROC.2018.2854372](#).
- [3] M. Asghari, “Silicon photonics: A low cost integration platform for datacom and telecom applications,” in *Proc. Conf. Opt. Fiber Commun./Nat. Fiber Opt. Eng. Conf.*, Feb. 2008, pp. 1–10.
- [4] F. Boeuf and K. Ouellette, “Industrialization of Si-photonics into a 300 mm CMOS fab,” in *Proc. Int. Symp. VLSI Technol., Syst. Appl. (VLSI-TSA)*, Taiwan, Apr. 2016, pp. 1–2, doi: [10.1109/VLSI-TSA.2016.7480504](#).
- [5] B. Jalali and S. Fathpour, “Silicon photonics,” *J. Lightw. Technol.*, vol. 24, no. 12, pp. 4600–4615, Dec. 2006, doi: [10.1109/JLT.2006.885782](#).
- [6] R. Soref and B. Bennett, “Electrooptical effects in silicon,” *IEEE J. Quantum Electron.*, vol. QE-23, no. 1, pp. 123–129, Jan. 1987, doi: [10.1109/JQE.1987.1073206](#).
- [7] K. Ogawa et al., “Fundamental characteristics and high-speed applications of carrier-depletion silicon Mach-Zehnder modulators,” *IEICE Electron. Exp.*, vol. 11, no. 24, 2014, Art. no. 20142010, doi: [10.1587/leex.11.20142010](#).
- [8] A. Liu et al., “High-speed optical modulation based on carrier depletion in a silicon waveguide,” *Opt. Exp.*, vol. 15, no. 2, pp. 660–668, Jan. 2007, doi: [10.1364/OE.15.000660](#).
- [9] L. Yang and J. Ding, “High-speed silicon Mach-Zehnder optical modulator with large optical bandwidth,” *J. Lightw. Technol.*, vol. 32, no. 5, pp. 966–970, Mar. 1, 2014, doi: [10.1109/JLT.2013.2295401](#).
- [10] J. Ding et al., “Ultra-low-power carrier-depletion Mach-Zehnder silicon optical modulator,” *Opt. Exp.*, vol. 20, no. 7, pp. 7081–7087, 2012, doi: [10.1364/OE.20.007081](#).
- [11] J. Fujikata et al., “High-speed and highly efficient Si optical modulator with strained SiGe layer,” *Appl. Phys. Exp.*, vol. 11, no. 3, Feb. 2018, Art. no. 032201, doi: [10.7567/APEX.11.032201](#).
- [12] Y. Kim, M. Takenaka, T. Osada, M. Hata, and S. Takagi, “Strain-induced enhancement of plasma dispersion effect and free-carrier absorption in SiGe optical modulators,” *Sci. Rep.*, vol. 4, no. 1, p. 4683, Apr. 2014.
- [13] M. Liu et al., “A graphene-based broadband optical modulator,” *Nature*, vol. 474, no. 7349, pp. 64–67, Jun. 2011, doi: [10.1038/nature10067](#).
- [14] Y. T. Hu et al., “Broadband 10 Gb/s graphene electro-absorption modulator on silicon for chip-level optical interconnects,” in *IEDM Tech. Dig.*, San Francisco, CA, USA, Dec. 2014, pp. 5.6.1–5.6.4, doi: [10.1109/IEDM.2014.7046991](#).
- [15] M. Lipson, “Optical modulator based on transition-metal dichalcogenides (TMDs),” in *Proc. Opt. Fiber Commun. Conf. Exhib. (OFC)*, San Francisco, CA, USA, Jun. 2021, pp. 1–4.
- [16] I. Datta et al., “Low-loss composite photonic platform based on 2D semiconductor monolayers,” *Nature Photon.*, vol. 14, no. 4, pp. 256–262, Apr. 2020, doi: [10.1038/s41566-020-0590-4](#).
- [17] F. Eltes et al., “A BaTiO₃-based electro-optic poekels modulator monolithically integrated on an advanced silicon photonics platform,” *J. Lightw. Technol.*, vol. 37, no. 5, pp. 1456–1462, Mar. 1, 2019, doi: [10.1109/JLT.2019.2893500](#).
- [18] C. Wang, M. Zhang, B. Stern, M. Lipson, and M. Lončar, “Nanophotonic lithium niobate electro-optic modulators,” *Opt. Exp.*, vol. 26, no. 2, pp. 1547–1555, Jan. 2018, doi: [10.1364/OE.26.001547](#).
- [19] M. He et al., “High-performance hybrid silicon and lithium niobate Mach-Zehnder modulators for 100 Gbit s^{−1} and beyond,” *Nature Photon.*, vol. 13, no. 5, pp. 359–364, May 2019, doi: [10.1038/s41566-019-0378-6](#).
- [20] Y. Jia et al., “Pulsed laser deposition of ferroelectric potassium tantalate-niobate optical waveguiding thin films,” *Opt. Mater. Exp.*, vol. 8, no. 3, pp. 541–548, 2018, doi: [10.1364/OME.8.000541](#).
- [21] S. Kim, Y. Kim, Y. Ban, M. Pantouvakis, and J. Van Campenhout, “Simulation study of a monolithic III–V/Si V-groove carrier depletion optical phase shifter,” *IEEE J. Quantum Electron.*, vol. 56, no. 2, pp. 1–8, Apr. 2020, doi: [10.1109/JQE.2020.2971764](#).
- [22] I. Charlet, Y. Désières, D. Marris-Morini, and F. Boeuf, “Capacitive modulator design optimization using Si and strained-SiGe for datacom applications,” *IEEE J. Sel. Topics Quantum Electron.*, vol. 27, no. 3, pp. 1–8, May 2021, doi: [10.1109/JSTQE.2020.3028447](#).

- [23] T. Ghani et al., "A 90 nm high volume manufacturing logic technology featuring novel 45 nm gate length strained silicon CMOS transistors," in *IEDM Tech. Dig.*, Washington, DC, USA, Dec. 2003, pp. 11.6.1–11.6.3, doi: [10.1109/IEDM.2003.1269442](https://doi.org/10.1109/IEDM.2003.1269442).
- [24] N. Loubet et al., "A novel dry selective etch of SiGe for the enablement of high performance logic stacked gate-all-around nanosheet devices," in *IEDM Tech. Dig.*, San Francisco, CA, USA, Dec. 2019, pp. 11.4.1–11.4.4, doi: [10.1109/IEDM19573.2019.8993615](https://doi.org/10.1109/IEDM19573.2019.8993615).
- [25] L. Bogaert et al., "SiGe EAM-based transceivers for datacenter interconnects and radio over fiber," *IEEE J. Sel. Topics Quantum Electron.*, vol. 27, no. 3, pp. 1–13, May 2021, doi: [10.1109/JSTQE.2020.3027046](https://doi.org/10.1109/JSTQE.2020.3027046).
- [26] S. Lischke et al., "Ultra-fast germanium photodiode with 3-dB bandwidth of 265 GHz," *Nature Photon.*, vol. 15, no. 12, pp. 925–931, Dec. 2021, doi: [10.1038/s41566-021-00893-w](https://doi.org/10.1038/s41566-021-00893-w).
- [27] M. Takenaka et al., "Heterogeneous CMOS photonics based on SiGe/Ge and III–V semiconductors integrated on Si platform," *IEEE J. Sel. Topics Quantum Electron.*, vol. 23, no. 3, pp. 64–76, May 2017, doi: [10.1109/JSTQE.2017.2660884](https://doi.org/10.1109/JSTQE.2017.2660884).
- [28] M. Takenaka and S. Takagi, "Strain engineering of plasma dispersion effect for SiGe optical modulators," *IEEE J. Quantum Electron.*, vol. 48, no. 1, pp. 8–16, Jan. 2012, doi: [10.1109/JQE.2011.2176104](https://doi.org/10.1109/JQE.2011.2176104).
- [29] G. T. Reed, G. Mashanovich, F. Y. Gardes, and D. J. Thomson, "Silicon optical modulators," *Nature Photon.*, vol. 4, no. 8, pp. 518–526, Aug. 2010.
- [30] T. P. Dash, S. Dey, S. Das, J. Jena, E. Mohapatra, and C. K. Maiti, "Performance comparison of strained-SiGe and bulk-Si channel FinFETs at 7 nm technology node," *J. Micromech. Microeng.*, vol. 29, no. 10, Aug. 2019, Art. no. 104001, doi: [10.1088/1361-6439/ab31c8](https://doi.org/10.1088/1361-6439/ab31c8).
- [31] J. Fujikata et al., "High-performance Si optical modulator with strained p-SiGe layer and its application to 25 Gbps optical transceiver," in *Proc. IEEE 14th Int. Conf. Group IV Photon. (GFP)*, Berlin, Germany, Aug. 2017, pp. 25–26, doi: [10.1109/GROUP4.2017.8082178](https://doi.org/10.1109/GROUP4.2017.8082178).
- [32] M. Douix et al., "SiGe-enhanced Si capacitive modulator integration in a 300 nm silicon photonics platform for low power consumption," *Opt. Exp.*, vol. 27, no. 13, pp. 17701–17707, 2019, doi: [10.1364/OE.27.017701](https://doi.org/10.1364/OE.27.017701).
- [33] D. Feng et al., "High-speed GeSi electroabsorption modulator on the SOI waveguide platform," *IEEE J. Sel. Topics Quantum Electron.*, vol. 19, no. 6, pp. 64–73, Nov. 2013, doi: [10.1109/JSTQE.2013.2278881](https://doi.org/10.1109/JSTQE.2013.2278881).
- [34] J. Fujikata, M. Noguchi, J. Han, S. Takahashi, M. Takenaka, and T. Nakamura, "Record-high modulation-efficiency depletion-type Si-based optical modulator with in-situ B doped strained SiGe layer on Si waveguide for 1.3 μm ," in *Proc. 42nd Eur. Conf. Opt. Commun. (ECOC)*, Dusseldorf, Germany, Sep. 2016, pp. 1–3.
- [35] Y. Kim, J. Fujikata, S. Takahashi, M. Takenaka, and S. Takagi, "First demonstration of SiGe-based carrier-injection Mach–Zehnder modulator with enhanced plasma dispersion effect," *Opt. Exp.*, vol. 24, no. 3, pp. 1979–1985, 2016, doi: [10.1364/OE.24.001979](https://doi.org/10.1364/OE.24.001979).
- [36] Y. Kim, M. Takenaka, and S. Takagi, "Numerical analysis of carrier-depletion strained SiGe optical modulators with vertical p-n junction," *IEEE J. Quantum Electron.*, vol. 51, no. 4, pp. 1–7, Apr. 2015, doi: [10.1109/JQE.2015.2405931](https://doi.org/10.1109/JQE.2015.2405931).
- [37] T. Cao, Y. Fei, L. Zhang, Y. Cao, and S. Chen, "Design of a silicon Mach–Zehnder modulator with a U-type PN junction," *Appl. Opt.*, vol. 52, no. 24, p. 5941, Aug. 2013.
- [38] Y. Kim, T. Jin, and Y. Bae, "A comparative simulation study on lateral and L-shaped PN junction phase shifters for single-drive 50 Gbps lumped Mach–Zehnder modulators," *Jpn. J. Appl. Phys.*, vol. 60, no. 5, May 2021, Art. no. 052002, doi: [10.35848/1347-4065/abeedd](https://doi.org/10.35848/1347-4065/abeedd).
- [39] T. Y. L. Ang, C. E. Png, S. T. Lim, and J. R. Ong, "Silicon modulators with optimized vertical PN junctions for high-modulation-efficiency and low-loss in the O-band," *Proc. SPIE*, vol. 10537, pp. 42–49, Feb. 2018, doi: [10.1117/12.2290385](https://doi.org/10.1117/12.2290385).
- [40] M. R. Watts, W. A. Zortman, D. C. Trotter, R. W. Young, and A. L. Lentine, "Low-voltage, compact, depletion-mode, silicon Mach–Zehnder modulator," *IEEE J. Sel. Topics Quantum Electron.*, vol. 16, no. 1, pp. 159–164, Jan. 2010.
- [41] Y. Liu, S. Dunham, T. Baehr-Jones, A. E.-J. Lim, G.-Q. Lo, and M. Hochberg, "Ultra-responsive phase shifters for depletion mode silicon modulators," *J. Lightw. Technol.*, vol. 31, no. 23, pp. 3787–3793, Dec. 1, 2013.
- [42] Z. Yong et al., "U-shaped PN junctions for efficient silicon Mach–Zehnder and microring modulators in the O-band," *Opt. Exp.*, vol. 25, no. 7, pp. 8425–8439, Apr. 2017.
- [43] Y. Kim, M. Takenaka, T. Osada, M. Hata, and S. Takagi, "Fabrication and evaluation of propagation loss of Si/SiGe/Si photonic-wire waveguides for Si based optical modulator," *Thin Solid Films*, vol. 557, pp. 342–345, Apr. 2014, doi: [10.1016/j.tsf.2013.10.063](https://doi.org/10.1016/j.tsf.2013.10.063).
- [44] M. Nedeljkovic, R. Soref, and G. Z. Mashanovich, "Free-carrier electrorefraction and electroabsorption modulation predictions for silicon over the 1–14- μm infrared wavelength range," *IEEE Photon. J.*, vol. 3, no. 6, pp. 1171–1180, Dec. 2011, doi: [10.1109/JPHOT.2011.2171930](https://doi.org/10.1109/JPHOT.2011.2171930).
- [45] Y. Kim et al., "Proposal and simulation of a low loss, highly efficient monolithic III–V/Si optical phase shifter," in *Proc. IEEE 16th Int. Conf. Group IV Photon. (GFP)*, Singapore, Aug. 2019, pp. 1–2, doi: [10.1109/GROUP4.2019.8926128](https://doi.org/10.1109/GROUP4.2019.8926128).
- [46] X. Li et al., "Single-drive high-speed lumped depletion-type modulators toward 10 fJ/bit energy consumption," *Photon. Res.*, vol. 5, no. 2, pp. 134–142, 2017, doi: [10.1364/PRJ.5.000134](https://doi.org/10.1364/PRJ.5.000134).
- [47] Ngspice. Accessed: May 20, 2022. [Online]. Available: <http://ngspice.sourceforge.net/>
- [48] M. Streshinsky et al., "Low power 50 Gb/s silicon traveling wave Mach–Zehnder modulator near 1300 nm," *Opt. Exp.*, vol. 21, no. 25, pp. 30350–30357, 2013, doi: [10.1364/OE.21.030350](https://doi.org/10.1364/OE.21.030350).
- [49] T. Ferroiti et al., "Co-integrated 1.3 μm hybrid III–V/silicon tunable laser and silicon Mach–Zehnder modulator operating at 25 Gb/s," *Opt. Exp.*, vol. 24, no. 26, pp. 30379–30401, 2016, doi: [10.1364/OE.24.030379](https://doi.org/10.1364/OE.24.030379).
- [50] D. Perez-Galacho et al., "Low voltage 25Gbps silicon Mach–Zehnder modulator in the O-band," *Opt. Exp.*, vol. 25, no. 10, pp. 11217–11222, 2017, doi: [10.1364/OE.25.011217](https://doi.org/10.1364/OE.25.011217).
- [51] G. Zhou et al., "Silicon Mach–Zehnder modulator using a highly-efficient L-shape PN junction," *Proc. SPIE*, vol. 10964, Nov. 2018, Art. no. 1096419, doi: [10.1117/12.2505116](https://doi.org/10.1117/12.2505116).